Draft version November 3, 2026
Typeset using LaTeX **twocolumn** style in AASTeX7.0.1

arXiv:2611.00195v1 [astro-ph.GA] 30 Oct 2026

EMBER: A Little Red Dot Candidate at $z_{\rm spec} = 10.36$ in the Seed Black Hole Era

Takumi S. Tanaka, Hollis B. Akins, John D. Silverman, Caitlin M. Casey, Ezequiel Treister, Manuel Aravena, Yuichi Harikane, Benny Trakhtenbrot, Kohei Inayoshi, Kazuhiro Shimasaku, Maximilien Franco, Seiji Fujimoto, Mingyu Li, Hiroya Umeda, Jan-Torge Schindler, Akio K. Inoue, Jean-Baptiste Billand, Darshan Kakkad, Xuheng Ding, Steven L. Finkelstein, Michaela Hirschmann, Z. Ghaffari, Andrew J. Battisti, Lauro Moscardini, Nicole E. Drakos, Rasha M. Samir, Jeyhan S. Kartaltepe, Qinyue Fei, Ming-Yang Zhuang, Olivier Ilbert, Wuji Wang, Rafael C. Arango-Toro, Hiddo S. B. Algera, Greta Toni, Junya Arita, Kei Ito, Ghassem Gozaliasl, Dale D. Kocevski, Yunjing Wu, Masafusa Onoue, Marc Huertas-Company, Yiyang Zhang, Jason Rhodes, Andreas L. Faisst, Zihao Li, Crystal L. Martin, Makoto Ando, Vasily Kokorev, Sophie L. Newman, Can Xu, Suin Matsui, Jialai Wang, Carter Flayhart, Hossein Hatamnia, Ali Ahmad Khostovan, Ronaldo Laishram, Felix Martinez III, David B. Sanders, Sune Toft, Francesco Valentino And Jorge Zavala

(Affiliations can be found after the references)

ABSTRACT

Little red dots (LRDs) are a newly discovered population that may trace rapidly growing black holes (BHs) and provide a link between seed BHs and luminous active galactic nuclei (AGNs). However, no LRD had previously been spectroscopically confirmed at $z > 10$, leaving this earliest phase observationally unexplored. Using JWST/NIRSpec spectroscopy from the EMBER program, we measure a spectroscopic redshift of $z_{\rm spec} = 10.361^{+0.003}_{-0.002}$ for CW-LRD-z10, the highest-redshift LRD candidate known to date. The redshift is constrained by a prominent Lyα break and multiple tentative emission lines, including C IV $\lambda\lambda$1549, 1551 and [O III] λ4363 detected at $S/N = 3.9$ and 3.6, respectively. Its extreme NIRCam-MIRI color of $m_{\rm F444W} - m_{\rm F770W} = 1.82 \pm 0.1$, characteristic V-shaped continuum with a turnover near the Balmer limit, and continuum slopes of $\beta_{\rm UV} = -2.26^{+0.11}_{-0.11}$ and $\beta_{\rm opt} = 1.17^{+0.74}_{-0.70}$ all support its LRD nature. A possible iron complex at $\lambda_{\rm rest} \sim 0.24$ - $0.25\,\mu$m and a possibly high $\log$ ([O III] λ4363/Hγ) $= 0.17^{+0.24}_{-0.22}$ further support an AGN-like interpretation, as seen in previously known LRDs. Tentative detection of Lyα emission may indicate enhanced Lyα transmission at $z \sim 10$. Our findings extend the observational frontier of BH growth into the seed-BH formation era, and upcoming MIRI spectroscopy will further establish the physical nature of the source.

Keywords: Active galactic nuclei (16) — Galaxy evolution (594) — High-redshift galaxies (734)

1. INTRODUCTION

Supermassive black holes (SMBHs) are ubiquitous in massive galaxies in the local Universe and are thought to co-evolve with their host galaxies (e.g., J. Kormendy & L. C. Ho 2013). However, the origin of SMBHs remains one of the major unsolved problems in modern astrophysics (e.g., M. Volonteri 2010; K. Inayoshi et al. 2020; J. Regan & M. Volonteri 2024).

As a possible key population for uncovering the origin of SMBHs, "little red dots" (LRDs) have recently attracted significant attention (e.g., I. Labbé et al. 2023; L. J. Furtak et al. 2024; J. Matthee et al. 2024; D. D. Kocevski et al. 2023; Y. Harikane et al. 2023; G. Barro et al. 2024; H. B. Akins et al. 2025; K. N. Hainline et al. 2025; R. E. Hviding et al. 2025; K. Inayoshi & L. C. Ho 2025). LRDs were first revealed by *JWST* thanks to its unprecedented sensitivity at infrared wavelengths (J. Rigby et al. 2023) and are characterized by rest-optical compact morphologies and a unique V-shaped spectral energy distribution (SED), with a blue rest-UV component and a steep, red rest-optical component (e.g., I. Labbé et al. 2023; L. J. Furtak et al. 2024; J. Matthee et al. 2024; D. D. Kocevski et al. 2023; G. Barro et al. 2024; H. B. Akins et al. 2025). These components transition near the Balmer limit (e.g., D. J. Setton et al. 2025a) and often show a Balmer break (e.g., V. Kokorev et al. 2024; I. Labbe et al. 2024; B. Wang et al. 2025), and in some cases exhibit an extremely strong Balmer break that cannot be explained by stellar populations alone (e.g., A. de Graaff et al. 2025a; R. P. Naidu et al. 2026; A. J. Taylor et al. 2025).

Spectroscopic observations have revealed broad Balmer emission lines with absorption features in many LRDs (e.g., I. Labbe et al. 2025; L. J. Furtak et al. 2024; J. Matthee et al. 2024; J. E. Greene et al. 2024). Despite

having broad Balmer lines similar to those of type-I active galactic nuclei (AGN), LRDs show several unusual properties that distinguish them from typical AGNs. First, most LRDs are undetected in X-rays (M. Yue et al. 2024; T. T. Ananna et al. 2024; R. Maiolino et al. 2025; H. B. Akins et al. 2025), with rare exceptions including objects proposed to be in transition from LRDs to conventional AGNs (R. E. Hviding et al. 2026; S. Fu et al. 2026). LRDs are also generally undetected in radio (H. B. Akins et al. 2025; K. Perger et al. 2025; G. Mazzolari et al. 2026; A. J. Gloudemans et al. 2025), although radio emission has been detected in some low-z LRD analogs (L. F. Rodriguez & I. F. Mirabel 2026; L. F. Rodríguez et al. 2026). Recent studies have revealed hot-dust emission in individual LRDs and stacked samples (I. Delvecchio et al. 2025; X. Lin et al. 2026a; X. Ji et al. 2026a; P. G. Pérez-González et al. 2026; M. Brazzini et al. 2026). However, the detection of hot-dust emission does not necessarily imply that dust attenuation is responsible for the steep red rest-optical continua of LRDs, and the relative contributions of dust attenuation and other emission mechanisms remain uncertain (I. Delvecchio et al. 2025; D. J. Setton et al. 2025b). Many LRDs have not shown significant photometric variability (M. Kokubo & Y. Harikane 2025; Z. Zhang et al. 2025a; W. L. Tee et al. 2025; S. Zhou et al. 2025), although photometric variability has been reported in gravitationally lensed high-redshift LRDs in a century time-scale (Z. Zhang et al. 2025b) and low-z analogs (R. Lin et al. 2026). Multi-epoch observations have also revealed variations in broad Balmer-line equivalent widths and emission-line fluxes in individual LRDs (L. J. Furtak et al. 2025; X. Ji et al. 2025; E. Lambrides et al. 2026; M. Brooks et al. 2026; R. P. Naidu et al. 2026), whereas recent systematic monitoring studies have found substantially weaker Hα variability in LRDs than expected for typical AGNs (Z. Liu et al. 2026; Z. Stone et al. 2026). In summary, these unusual properties leave their physical nature uncertain.

One proposed framework is the BH envelope (or BH-star) model (e.g., R. P. Naidu et al. 2026; D. Kido et al. 2025; K. Inayoshi et al. 2026), in which a BH rapidly grows from a seed, possibly through super-Eddington accretion, while surrounded by dense, optically thick gas with an effective temperature of $\sim$ 4000 - 5000 K. The rest-optical-to-near-infrared SEDs of LRDs can be reproduced by blackbody-like emission from BH envelopes, whose Wien tails explain the steep rest-optical continua (e.g., X. Lin et al. 2026a; D. Kido et al. 2025; A. de Graaff et al. 2026; H. Umeda et al. 2026). Furthermore, dense, predominantly neutral gas ($n_{\rm H} \gtrsim 10^9\,{\rm cm}^{-3}$) can produce strong Balmer absorption and a Balmer break through collisional excitation of hydrogen to the $n = 2$ state (K. Inayoshi & R. Maiolino 2025; Z. Yan et al. 2026). However, the geometry and physical properties of the surrounding gas remain uncertain, and the gas may have a covering factor below unity, as in some clumpy, disk-like, or toroidal configurations (Y. Pang et al. 2026; M. Tang et al. 2026; X. Ji et al. 2026b; C.-H. Chen et al. 2026; S. Zhou et al. 2026; H. Yanagisawa et al. 2026). In addition, dense ionized gas with electron column densities of $N_{\rm e} \sim 10^{24}\,{\rm cm}^{-2}$ may contribute to broad Balmer-line profiles through electron scattering (V. Rusakov et al. 2025), suggesting that the emitting, absorbing, and scattering regions may not be identical. Other models invoke nebular emission from ionized gas cocoons (A. Sneppen et al. 2026a,b), dense accretion flows around direct-collapse BHs (F. Pacucci et al. 2026), or dust-reddened AGN emission (P. Madau & R. Maiolino 2026; P. Madau et al. 2026) to explain the characteristic red rest-optical continua of LRDs. Therefore, we have not yet achieved a unified model of the nature of LRDs.

Regardless of the specific physical framework invoked to explain their unusual properties, LRDs may trace an early stage of BH growth, potentially close to the epoch of BH seeding. This picture is supported by K. Inayoshi (2025), who compared the number density evolution of LRDs with that of non-LRD AGNs and suggested that LRDs may represent the first episode of BH growth after seed BH formation. Therefore, LRDs provide a crucial population for observationally probing seed BHs, which have long been a theoretical target of study (M. Volonteri 2010; K. Inayoshi et al. 2020; J. Regan & M. Volonteri 2024). However, almost all previous LRD studies have been limited to $z < 9$. Prior to this work, the most distant LRD with a spectroscopic redshift was CAPERS-LRD-z9 at $z = 9.288$ with a broad Hβ detection (A. J. Taylor et al. 2025). More recently, X. Cai et al. (2026) reported a broad-line AGN at $z = 9.984$ and discussed its possible classification as an LRD. Extending LRD studies to $z > 10$ is crucial for constraining their number-density evolution during their emergence and for uncovering when and through which mechanisms seed BHs formed, a regime that has remained observationally inaccessible until now.

As shown in Figure 1 of T. S. Tanaka et al. (2025), searching for $z > 10$ LRDs requires the mid-infrared coverage provided by MIRI to sample their steep rest-optical slope and distinguish LRDs from galaxies. Motivated by this, T. S. Tanaka et al. (2025) developed a joint NIRCam-MIRI color selection method and applied it to the COSMOS-Web imaging data (GO#1727, PIs J. Kartaltepe and C. M. Casey; C. M. Casey et al. 2023) and identified a promising candidate for the first $z > 10$ LRD, CW-LRD-z10, with a photometric redshift

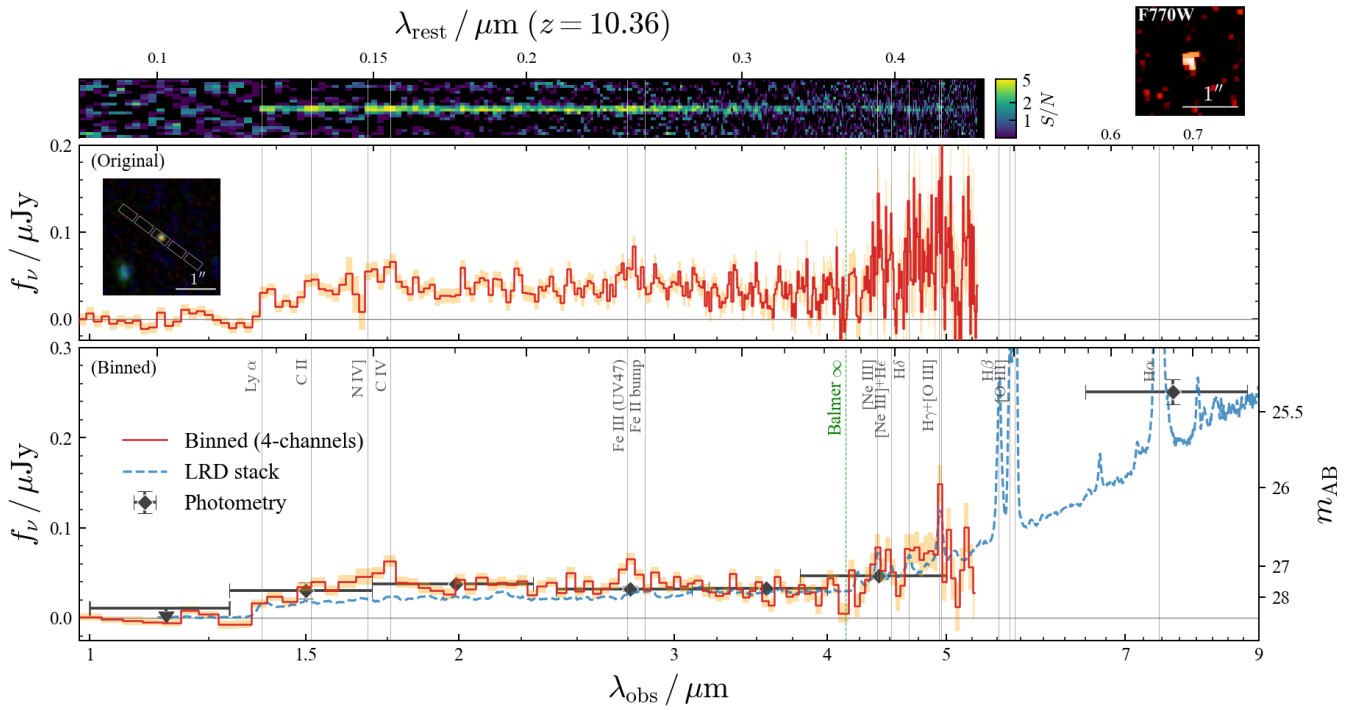


Figure 1. *JWST*/NIRSpec PRISM spectrum of CW-LRD-z10. The top panel shows the nod-subtracted 2D spectrum produced by the *JWST* science calibration pipeline. The middle panel shows the optimally extracted 1D spectrum, and the bottom panel compares the spectrum, binned by taking the inverse-variance-weighted average over every four spectral channels, with the photometry reported in T. S. Tanaka et al. (2025). Uncertainties (1σ) are shown as the orange shaded region. The inset in the middle panel shows the NIRCam $3'' \times 3''$ RGB (R: F356W+F444W; G: F200W+F277W; B: F115W+F150W) image overlaid with the NIRSpec slitlet, while the upper-right inset shows a $2'' \times 2''$ F770W image. In the bottom panel, we overplot a stacked spectrum of 274 LRDs compiled from the EMBER survey and archival observations with the dashed line (H. B. Akins et al. *in prep.*), scaled to match the continuum of CW-LRD-z10 over $\lambda_{\rm rest} = 0.28$ - $0.32\,\mu$m. The spectrum exhibits the Lyα break at ~ 1.3 - $1.4\,\mu$m and a slight upturn redward of $\sim 4.2\,\mu$m, consistent with a V-shaped SED of typical LRDs redshifted to $z \sim 10$.

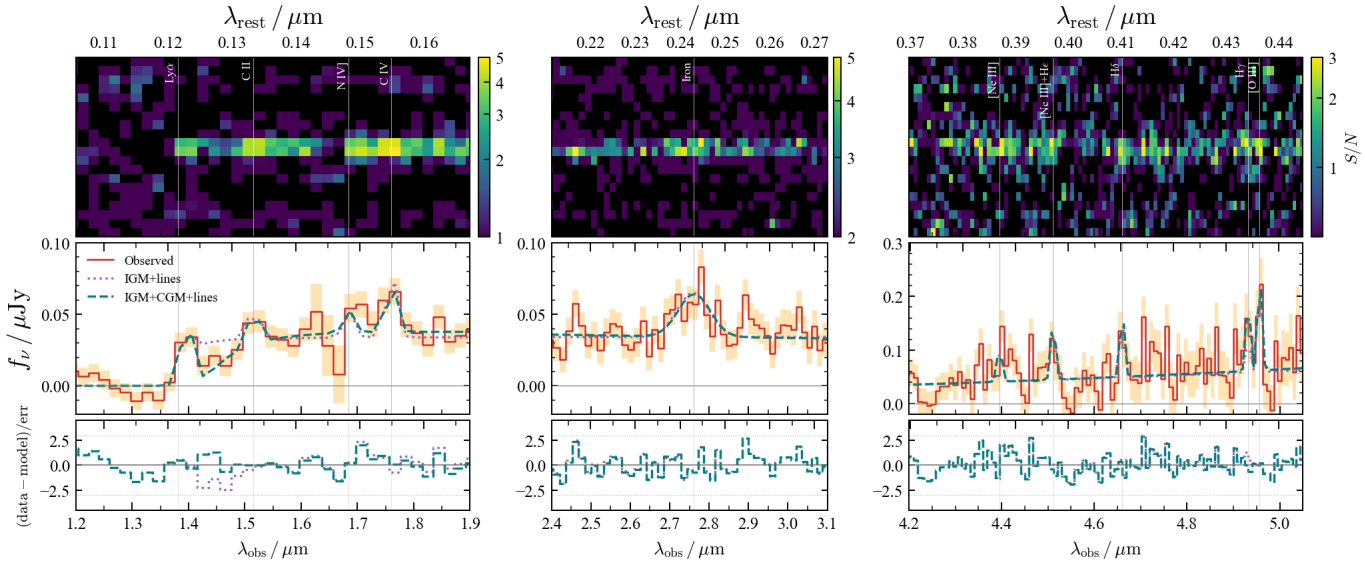


Figure 2. Zoomed-in versions of Figure 1 including emission lines. The middle rows show the unbinned original resolution spectrum and two fitted model SEDs: IGM+lines (dotted) and IGM+CGM+lines (dashed). The bottom panels show the residuals normalized by the 1σ uncertainties. We identify multiple line features with $S/N \sim 2$ - 4 at wavelengths consistent with $z_{\rm spec} = 10.36$.

of $z_{\rm phot} = 10.5^{+0.7}_{-0.6}$. They used this candidate to place the first constraint on the abundance of LRDs at $z \sim 10$, $\Phi_{\rm LRD} = \left(1.2^{+2.7}_{-1.0}\right) \times 10^{-6}\,{\rm Mpc^{-3}\,mag^{-1}}$ for $M_{\rm UV} = -20$, suggesting the redshift evolution of their number density following the log-normal evolution hypothesized by K. Inayoshi (2025). However, CW-LRD-z10 had not yet been spectroscopically confirmed, leaving both its nature and the inferred $z \sim 10$ LRD abundance dependent on the photometric interpretation.

In this paper, we report NIRSpec spectroscopic observations of CW-LRD-z10. In Section 2, we describe the data. In Sections 3 and 4, we present the spectroscopic analysis and the results, respectively. Then Section 5 discusses the nature of CW-LRD-z10, and Section 6 provides the summary. Throughout this work, we assume a flat ΛCDM cosmology with $H_0 = 67.4\,{\rm km\,s^{-1}\,Mpc^{-1}}$, $\Omega_{\rm m} = 0.315$, and $\Omega_\Lambda = 0.685$ (Planck Collaboration et al. 2020).

2. DATA

CW-LRD-z10 at (R.A., Decl.) = ($10^{\rm h}00^{\rm m}20^{\rm s}.1836$, $+02°27'14.''022$) was observed with *JWST*/NIRSpec Multi-Object Spectroscopy as part of the Early Massive Black Hole Evolution & Reddening (EMBER) program (GO#7076, PI H. Akins). EMBER was designed to conduct a comprehensive spectroscopic census of the brightest LRDs selected across multiple extragalactic fields. While the highest priority EMBER targets were bright ($m_{\rm F444W} < 24$) $z \sim$ 3–7 LRDs, CW-LRD-z10 was selected for observation based on its robust photometric redshift of $z_{\rm phot} = 10.5^{+0.7}_{-0.6}$ and previous identification as an LRD candidate based on MIRI photometry (T. S. Tanaka et al. 2025). CW-LRD-z10 was observed as part of Observation 1 of the EMBER program on November 27, 2025, with on-source exposure times of 1.48 hr using the PRISM/CLEAR disperser/filter pair (0.6 - 5.3 μm, $R \sim 100$) and 0.92 hr using G395M/F290LP (2.87 - 5.10 μm, $R \sim 1000$).

We process the NIRSpec data starting from the uncalibrated `uncal` products using version 1.20.2 of the *JWST* Calibration Pipeline (H. Bushouse et al. 2023) and the Calibration Reference Data System (CRDS) mapping pmap-1481. The reduction follows the standard workflow implemented by the pipeline, with a few modifications to improve the data quality (described in more detail in H. B. Akins et al. *in prep*). First, following the detector-level corrections applied in stage 1, we employ a custom iterative procedure to subtract the thermal "picture frame" effect and $1/f$ noise on the detector, masking spectral traces from all open micro-shutter assembly (MSA) shutters. The picture frame subtraction uses the recently released CRDS `pictureframe` reference file, and is particularly important for reliable background subtraction. We extract the 2D spectra for CW-LRD-z10 from each nod in stage 2 and apply flat-field, photometric calibration, and wavelength calibration. We inspect each nod to ensure that no shutters were stuck closed, and then perform the standard nodded background subtraction and combination of the individual exposures into rectified products. We extract a 1D spectrum from the combined 2D product using the optimal-extraction method of K. Horne (1986) with a profile constructed as the median of the rectified 2D spectrum along the cross-dispersion direction. We note that the G395M spectrum for CW-LRD-z10 is contaminated by the spectral trace from a nearby bright object, as G395M spectra were allowed to overlap in the MSA design. Given the contamination and the faint nature of this source, the analysis here focuses only on the deeper PRISM spectrum. We present the processed NIRSpec/PRISM spectrum in Figure 1. The spectrum is consistent with the observed photometry, supporting the robustness of the pipeline slit-loss correction.

3. SPECTROSCOPIC FITTING

To derive the spectroscopic redshift and characterize CW-LRD-z10, we perform Markov Chain Monte Carlo spectrum fitting using `emcee` (D. Foreman-Mackey et al. 2013). For the intrinsic continuum, we adopt a broken power law (BPL) with independent rest-frame UV and optical slopes, $\beta_{\rm UV}$ and $\beta_{\rm opt}$ ($f_\lambda \propto \lambda^\beta$). The two power laws are joined continuously at a turnover rest-frame wavelength, $\lambda_{\rm turn}$, and the overall normalization is parameterized by the absolute magnitude in rest-frame 1450 Å ($M_{\rm UV}$). To test whether the BPL model is required, we additionally fit a single power-law (SPL) continuum and compare the goodness of fit using the Bayesian information criterion (BIC).

We include Gaussian emission lines for Lyα, C II λ1335, N IV] $\lambda\lambda$1483, 1487, C IV $\lambda\lambda$1549, 1551, [Ne III] λ3869, [Ne III] λ3967 + Hϵ, Hδ, Hγ, and [O III] λ4363. Because these lines are unresolved at the spectral resolution of NIRSpec/PRISM, their observed profiles are modeled using a Gaussian line-spread function (LSF) with a wavelength-dependent resolution for a point source provided by the `unite` package ($R \sim 50$ - 500; R. E. Hviding 2026). This prescription assumes a point source centered in an MSA shutter, which is a reasonable approximation for the observation of CW-LRD-z10 (Figure 1), and accounts for the higher effective spectral resolution of compact sources compared to the nominal resolution derived assuming uniform illumination across the shutter (e.g., see A. de Graaff et al. 2024). Note that, at the fitted spectroscopic

Table 1. Estimated properties of CW-LRD-z10 from the spectral fits.

Model			$z_{\rm spec}$	$M_{\rm UV}$	$\beta_{\rm UV}$	$\beta_{\rm opt}$	$\lambda_{\rm turn}$	$\log R_{\rm b}$	$\log N_{\rm HI}$	ΔBIC*
Continuum	Absorption	Lines†					[μm]	[cMpc]	[cm^{-2}]	
BPL	IGM+CGM	Included	$10.361^{+0.003}_{-0.002}$	$-20.16^{+0.07}_{-0.07}$	$-2.26^{+0.11}_{-0.11}$	$1.17^{+0.74}_{-0.70}$	$0.356^{+0.010}_{-0.013}$	$0.42^{+1.04}_{-0.97}$	$22.81^{+0.20}_{-0.25}$	—
BPL	IGM	Included	$10.361^{+0.003}_{-0.002}$	$-20.01^{+0.05}_{-0.05}$	$-2.03^{+0.08}_{-0.08}$	$1.01^{+0.71}_{-0.69}$	$0.359^{+0.011}_{-0.013}$	$0.65^{+0.63}_{-1.10}$	—	2.6
BPL	IGM+CGM	Lyα only	$10.41^{+0.06}_{-0.06}$	$-20.13^{+0.07}_{-0.08}$	$-2.20^{+0.12}_{-0.12}$	$1.09^{+0.77}_{-0.70}$	$0.355^{+0.012}_{-0.014}$	$0.56^{+1.10}_{-1.06}$	$22.52^{+0.31}_{-0.53}$	—
BPL	IGM	Lyα only	$10.32^{+0.16}_{-0.09}$	$-20.00^{+0.05}_{-0.06}$	$-2.03^{+0.08}_{-0.09}$	$1.02^{+0.80}_{-0.75}$	$0.362^{+0.013}_{-0.016}$	$0.38^{+1.08}_{-0.95}$	—	—
SPL	IGM+CGM	Included	$10.361^{+0.002}_{-0.002}$	$-20.05^{+0.07}_{-0.07}$	$-2.01^{+0.11}_{-0.10}$	—	—	$0.46^{+0.96}_{-0.97}$	$22.56^{+0.28}_{-0.42}$	17.7

† (Included) The following emission lines are modeled with Gaussian profiles: Lyα, C II λ1335, N IV] $\lambda\lambda$1483, 1487, C IV $\lambda\lambda$1549, 1551, an iron complex (Fe II UV bump or Fe III UV47 multiplet), [Ne III] λ3869, [Ne III] λ3967 + Hϵ, Hδ, Hγ, and [O III] λ4363. (Lyα only) Only Lyα is included in the model, and the corresponding wavelength regions for the other lines are masked.

* BIC difference compared to the broken power-law model with the IGM+CGM absorption and the lines. The BIC differences are not calculated for models without emission lines, as the corresponding wavelength regions are masked during fitting.

Table 2. Estimated line fluxes and equivalent widths of CW-LRD-z10 from the fitting with the BPL model including IGM+CGM absorption and emission lines.

Line	$F_{\rm line}/10^{-20}$	$S/N_{\rm line}$	EW$_{\rm rest}$
	[erg s^{-1} cm^{-2}]		[Å]
Lyα	243^{+40}_{-51}	4.2	$34.1^{+6.6}_{-7.3}$
C II λ1335	$73.5^{+30.6}_{-29.2}$	2.5	$12.4^{+5.2}_{-5.1}$
N IV] $\lambda\lambda$1483, 1487	$46.9^{+26.8}_{-25.2}$	1.9	$10.0^{+6.0}_{-5.4}$
C IV $\lambda\lambda$1549, 1551	$94.3^{+23.7}_{-24.4}$	3.9	$22.2^{+6.1}_{-5.9}$
Iron complex	$121.4^{+27.5}_{-27.2}$	4.4	$79.2^{+18.8}_{-18.7}$
[Ne III] λ3869	$14.8^{+6.9}_{-6.3}$	2.2	$20.7^{+9.7}_{-9.1}$
[Ne III] λ3967 + Hϵ	$14.9^{+6.3}_{-6.1}$	2.4	$20.0^{+8.9}_{-8.5}$
Hδ	$16.6^{+6.2}_{-6.8}$	2.6	$21.6^{+8.6}_{-9.0}$
Hγ	$17.8^{+7.4}_{-7.1}$	2.5	$21.4^{+10.2}_{-8.6}$
[O III] λ4363	$26.5^{+7.0}_{-7.8}$	3.6	$31.8^{+9.7}_{-9.8}$

NOTE— The quoted uncertainties correspond to the 16th–84th percentile ranges of the posterior distributions. All lines except the iron complex and Lyα are assumed to be unresolved, with their observed widths determined by the wavelength-dependent NIRSpec/PRISM line-spread function. The iron complex is treated as a resolved feature, with a fitted effective rest-frame central wavelength of $0.2432^{+0.0011}_{-0.0010}$ μm and an intrinsic FWHM of $1.22^{+0.58}_{-0.32} \times 10^4$ km s^{-1}.

redshift of $z_{\rm spec}$ = 10.36 (Section 4.1), [O III] λ4363 and Hγ are observed near $\lambda_{\rm obs} \simeq 5\,\mu$m, where the PRISM resolving power reaches $R \sim 450$ based on the `unite` LSF, corresponding to a rest-frame spectral resolution of $\Delta\lambda_{\rm rest} \sim 10$ Å. Therefore, [O III] λ4363 and Hγ, separated by ~ 23 Å in the rest frame, are spectrally distinguishable in principle.

Given the limited spectral resolution of PRISM, we fit the unresolved N IV] $\lambda\lambda$1483, 1487 and C IV $\lambda\lambda$1549, 1551 doublets with a single Gaussian profile each, and tie the centroids of all lines except Lyα and the iron complex to a common systemic redshift without allowing individual velocity offsets. Thus, the only free parameter for each of these unresolved lines is its line flux. Note that the iron complex, which likely consists of a blend of multiple iron emission lines, is treated separately, and both its intrinsic FWHM and effective rest-frame central wavelength are fitted as free parameters.

Lyα is also treated separately, and both its intrinsic FWHM and velocity offset are fitted as free parameters. We consider two model setups: (i) only intergalactic medium (IGM) absorption and (ii) both IGM and circumgalactic medium (CGM) Lyα absorption. IGM absorption is modeled following the formalism of T. Totani et al. (2006), which is based on J. Miralda-Escudé (1998), with two free parameters: the neutral hydrogen fraction $x_{\rm HI}$ and the ionized bubble radius $R_{\rm b}$. Note that, following H. Umeda et al. (2024), we fix the redshift corresponding to the end of reionization at $z_{\rm end} = 5$ and neglect the contribution of neutral IGM at $z < z_{\rm end}$ to the damping-wing absorption. We confirm that varying $z_{\rm end}$ between 5 and 6 has a negligible effect on the fitting results. For the CGM, we assume a Voigt absorption profile with three free parameters: the neutral hydrogen column density $\log(N_{\rm HI})$, the velocity offset of the CGM from the galaxy Δv, and the velocity dispersion of the CGM $\sigma_{\rm CGM}$.

We also fit an emission feature that possibly corresponds to an iron complex around $\lambda_{\rm rest} \sim 0.24$ - $0.25\,\mu$m (see also Section 4.5). Since the individual lines are blended and cannot be resolved, we model the entire feature with a single Gaussian profile, treating its FWHM and central wavelength as free parameters. We confirm that the overall feature can be adequately reproduced by a single broad Gaussian with FWHM $\simeq 1.22^{+0.58}_{-0.32} \times 10^4$ km s^{-1} at the central wavelength of $\lambda_{\rm rest} = 0.2432^{+0.0011}_{-0.0010}\,\mu$m. We emphasize that

the primary purpose of this fit is to assess the significance of the iron-complex detection by using the integrated flux derived from the fitted Gaussian component, and the fitted line width is not assigned any physical interpretation. The best-fit SEDs are shown in Figure 2, and the fitted parameters are shown in Tables 1 and 2.

4. RESULTS

4.1. *Spectroscopic redshift*

The derived redshift is $z_{\rm spec} = 10.361^{+0.003}_{-0.002}$ from both the IGM+lines and the IGM+CGM+lines models, consistent with each other and with the previous photometric redshift, $z_{\rm phot} = 10.5^{+0.7}_{-0.6}$ (T. S. Tanaka et al. 2025). These tight constraints are largely driven by the tentative line features discussed in Section 4.3.

Independently of these lines, the spectrum also exhibits a clear break feature around $\lambda_{\rm obs} \sim 1.4\,\mu$m, which corresponds to the Lyα break. CW-LRD-z10 is undetected blueward of the break, while the continuum is detected at a signal-to-noise ratio of $S/N \sim 4$-5 redward of the break. To assess the redshift constraint primarily from the continuum break, we repeat the fit after masking the wavelength regions of the tentative line detections. Note that Lyα is left unmasked and remains included in the model, because masking the Lyα region would also remove the Lyα break. As shown in Table 1, the derived redshifts from the IGM and the IGM+CGM models, $10.32^{+0.16}_{-0.09}$ and $z_{\rm spec} = 10.41^{+0.06}_{-0.06}$, respectively, are consistent with $z_{\rm spec}$ obtained including the lines.

Note that this break cannot be interpreted as a Balmer break at $z \sim 3$. When combined with the non-detections in filters blueward of $1.4\,\mu$m, the implied break strength, defined as the f_ν ratio across the break, is $\gtrsim 10$. Such an extreme Balmer break is far stronger than expected for a conventional post-starburst galaxy, for which the Balmer break strength is typically $\lesssim 3$. We also confirm this by fitting the photometry with $z = 3$-4 galaxy models using `Prospector` (B. D. Johnson et al. 2021). The best-fit model SED predicts a continuum flux density of $\sim 0.02\,\mu$Jy at $\lambda_{\rm obs} < 1.5\,\mu$m, which is inconsistent with both the observed spectrum and the photometric upper limits, e.g., F115W < 3.3 nJy (2σ upper limit by T. S. Tanaka et al. 2025). Although similarly extreme Balmer breaks have been reported in some LRDs (R. P. Naidu et al. 2026; A. de Graaff et al. 2025a; A. J. Taylor et al. 2025), an LRD-like solution at $z \sim 3$ is also disfavored by the absence of strong rest-optical emission lines, such as Hα. Furthermore, the continuum slope at $\lambda_{\rm obs} > 1.5\,\mu$m, $\beta = -2.01^{+0.11}_{-0.10}$ from the SPL fit, is substantially bluer than the rest-optical slopes expected for LRDs, for example $\beta_{\rm opt} > 0$ (D. D. Kocevski et al. 2025) or $\beta_{\rm opt} > -0.52$ (D. D. Kocevski et al. 2026).

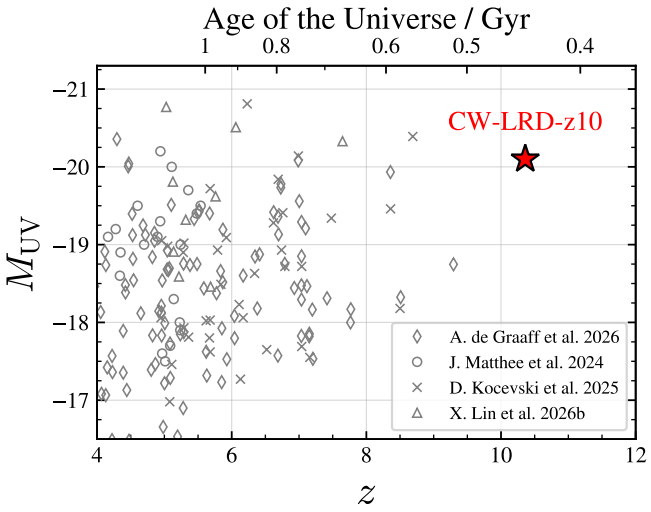


Figure 3. UV absolute magnitudes ($M_{\rm UV}$) of previously spectroscopically confirmed LRDs (J. Matthee et al. 2024; D. D. Kocevski et al. 2025; X. Lin et al. 2026b; A. de Graaff et al. 2026) as a function of redshift. Note that there can be an overlap between different studies. The red star indicates CW-LRD-z10 (this study), representing the first LRD candidate with $z_{\rm spec} > 10$, corresponding to a cosmic age of < 0.5 Gyr.

Therefore, we conclude that CW-LRD-z10 is at $z_{\rm spec} = 10.36$, which establishes CW-LRD-z10 as the first $z_{\rm spec} > 10$ LRD candidate. The obtained UV absolute magnitude of $M_{\rm UV} = -20.16^{+0.07}_{-0.07}$ places it among the most luminous LRDs (Figure 3). It is substantially brighter than the only previously published LRD at $z_{\rm spec} > 9$, CAPERS-LRD-z9, at $z = 9.288$ and $M_{\rm UV} = -18.2 \pm 0.2$ (A. J. Taylor et al. 2025).

4.2. *Spectroscopic confirmation of a V-shaped SED*

The fit with the BPL continuum with IGM+CGM absorption and emission lines results in $\beta_{\rm UV} = -2.26^{+0.11}_{-0.11}$ and $\beta_{\rm opt} = 1.17^{+0.74}_{-0.70}$. Both of the fitted spectral slopes, as well as their large difference across the turnover, are consistent with those typically observed in lower-z LRDs (e.g., D. D. Kocevski et al. 2025; A. de Graaff et al. 2026; G. Barro et al. 2026; M. Ando et al. 2026). Furthermore, the BPL model is strongly favored over the SPL model with $\beta = -2.01^{+0.11}_{-0.10}$ by the BIC improvement of $\Delta{\rm BIC} = 17.7 > 10$, a conventional threshold for strong evidence in model selection, confirming a significant change in the continuum slope. This continuum-slope change is more clearly visible in the 4-channel binned spectrum (Figure 1, lower). Furthermore, the fitted turnover wavelength is $\lambda_{\rm turn} = 0.356^{+0.010}_{-0.013}\,\mu$m, which is consistent with the Balmer limit ($\lambda_{\rm rest} = 0.3646\,\mu$m) within the uncertainties, as commonly seen in LRDs (e.g., D. J. Setton et al. 2025a; A. de Graaff et al. 2026).

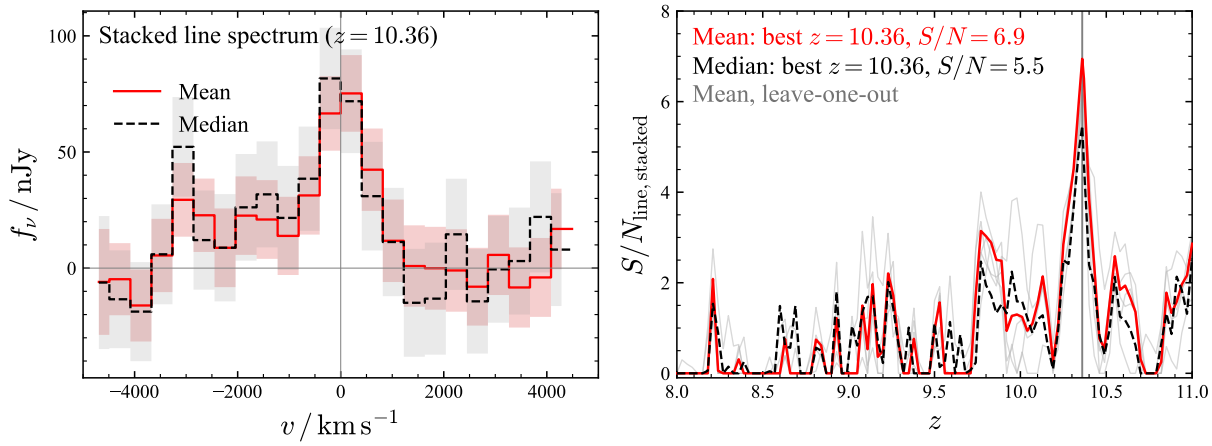


Figure 4. (Left) Continuum-subtracted stacked spectrum of [Ne III] λ3869, [Ne III] λ3967 + Hϵ, Hδ, Hγ, and [O III] λ4363 assuming z = 10.36. The red solid and black dashed lines show mean- and median-stacked spectra, respectively. 1σ uncertainties are shown as the shaded regions. (Right) S/N from the Gaussian fitting when redshift is varied. The gray thin lines indicate the results from the leave-one-out test. The stack S/N peaks at $z \sim 10.36$, providing additional support for $z_{\rm spec}$ = 10.36.

The UV-to-optical continuum shape and characteristic V-shape turnover in CW-LRD-z10 are consistent with typical LRDs at lower redshift. In the bottom panel of Figure 1, we overplot a stack of PRISM spectra of 274 LRDs from $z \sim$ 2.3–9.3, combining the EMBER survey with PRISM spectra from the ZENITH program (GO#7417, PIs C. Casey, H. B. Akins, and M. Franco) and archival observations from CAPERS (GO#6368, A. J. Taylor et al. 2025), RUBIES (GO#4233, A. de Graaff et al. 2025b), and other archival programs. The details of the LRD selection and stacking procedure will be provided in H. B. Akins et al. (*in prep*). The stacked spectrum shows a clear turnover at the Balmer limit, similar to CW-LRD-z10, and continues to rise toward redder wavelengths, consistent with the observed F770W photometry of CW-LRD-z10.

Moreover, CW-LRD-z10's Balmer-break strength, defined as the ratio of the continuum flux densities across the Balmer limit, is

$$\frac{\langle f_\nu \rangle_{4000\text{-}4100\,\text{Å}}}{\langle f_\nu \rangle_{3620\text{-}3720\,\text{Å}}} = 1.22^{+0.45}_{-0.35}. \quad (1)$$

This value is comparable to those commonly observed in LRDs at $z \sim$ 4-7 (A. de Graaff et al. 2026) and the value from the stacked spectrum ($\sim$ 1.6). However, the measured ratio is consistent with unity within a 1σ uncertainty and does not provide significant evidence for a Balmer break. Nevertheless, spectral fitting over a broader wavelength range strongly favors a broken power-law continuum, with different UV and optical slopes joined near the Balmer limit. We therefore conclude that the characteristic V-shaped continuum is still supported by the spectrum.

4.3. *Detection of rest-UV and optical lines*

Based on the spectroscopic fitting, we detect multiple emission-line features at the $S/N \sim$ 2-4 level. Other than Lyα (Section 4.6), C IV $\lambda\lambda$1549, 1551 and [O III] λ4363 show the highest values with S/N = 3.9 and 3.6, respectively.

To test these tentative line detections, we perform spectral stacking of these lines. After subtracting the fitted BPL continuum, we stack the residual spectrum around five rest-optical lines, [Ne III] λ3869, [Ne III] λ3967 + Hϵ, Hδ, Hγ, and [O III] λ4363 (Figure 4 left), in the velocity plane within $v \in [-5000, 5000]$ km s^{-1}. In the stacking process, other lines within the extracted velocity range are masked within a $\pm$1000 km s^{-1} window, and we construct both an inverse-variance-weighted mean stack and a median stack. We repeat this stacking over a redshift range of z = 8-11 and fit the stacked spectrum with a Gaussian centered at v = 0 to evaluate its S/N. Note that we use the stacked S/N as a consistency check between each line rather than as an independent global detection significance. We do not include the rest-UV lines shown in Figure 2 left (Lyα, C II λ1335, N IV] $\lambda\lambda$1483, 1487, and C IV $\lambda\lambda$1549, 1551) in the stacking analysis, because they have a much lower spectral resolution than optical lines.

The stacked signals from the mean and median stacking methods reach their maximum significance at z = 10.36, with S/N = 6.9 and 5.5 for mean and median, respectively (Figure 4). As a robustness check, we perform a leave-one-out test by repeating the stacking analysis five times, excluding one of the five lines in each realization. The stacked excess with S/N = 6.2-6.4 at z = 10.36 remains present in all cases, indicating that the stacking result is not driven by any single feature. Therefore, we

conclude that these tentative detections are unlikely to be coincidental and support the fitted spectroscopic redshift of $z_{\rm spec} = 10.36$.

4.4. *Line diagnostics*

Among the line-flux ratios accessible from the detected lines, O3Hg $\equiv \log$ ([O III] λ4363/Hγ) provides an important diagnostic of the nature of the ionizing source. [O III] λ4363 is sensitive to the electron temperature and the O3Hg ratio can be enhanced by the hard ionizing radiation field produced by an AGN (e.g., J. Gutkin et al. 2016; A. Feltre et al. 2016; G. Mazzolari et al. 2024). Some studies (e.g., J. Gutkin et al. 2016; A. Feltre et al. 2016; G. Mazzolari et al. 2024; C. L. Martin et al. 2026) have also used line diagnostics involving O3Hg in combination with line ratios such as O33 ([O III] λ5007/[O III] λ4363), O32 ([O III] λ5007/[O II] $\lambda\lambda$3727, 3729), and Ne3O2 ([Ne III] λ3869/[O II] λ3727) for discussing the nature of the ionizing source. However, the limited depth and wavelength coverage of the available data result in a marginal detection of [Ne III] λ3869 ($S/N = 2.2$), a non-detection of [O II] $\lambda\lambda$3727, 3729, and no coverage of [O III] λ5007.

The O3Hg ratio derived from the posterior samples is O3Hg $= 0.17^{+0.24}_{-0.22}$. This value is higher than those measured from stacked spectra of LRDs, LBDs (S. Geris et al. 2026), and broad-line AGNs (I. Juodžbalis et al. 2025) observed with JWST, and is relatively high even among measurements for individual LRDs (P. Rinaldi et al. 2024; G. C. Jones et al. 2026; M. Brazzini et al. 2026; X. Ji et al. 2026a). It is consistent with the values expected from AGN-only models over a wide range of O32$\lesssim 2$ and Ne3O2$\lesssim 1$ (Figure 5). We also estimate a 3σ upper limit on the [O II] $\lambda\lambda$3727, 3729 flux using mock spectra and obtain $F_{\rm [O\,II]} < 1.73 \times 10^{-19}$ erg s^{-1} cm^{-2}. Combining this upper limit with the 16th percentile of the [Ne III] λ3869 flux posterior, we derive a conservative lower limit of Ne3O2 > -0.31. This constraint is consistent with the AGN-only region of the diagnostic diagram over a wide range of plausible Ne3O2 values (Figure 5). However, neither of these line diagnostics rule out ionization by star formation.

The observed Hγ/Hδ flux ratio Hγ/H$\delta = 1.07^{+0.95}_{-0.47}$ is lower than the value expected for Case B recombination, which is $\simeq 1.8$ for $T_{\rm e} = 1\times10^4$ K and $n_{\rm e} = 1\times10^2$ cm^{-3}. This discrepancy cannot be explained by dust attenuation, since dust would preferentially suppress Hδ relative to Hγ and therefore increase the Hγ/Hδ ratio. Previous studies have discussed that Balmer-line ratios in the dense gas associated with LRDs may deviate from the Case B recombination predictions owing to high-density radiative-transfer effects (e.g., G. P. Nikopoulos et al. 2026; S.-J. Chang et al. 2026). According to Table 2 of G. P. Nikopoulos et al. (2026), JADES-GN-1181_73488 and CEERS-EGS-1345_1244 show Hγ/Hδ flux ratios of $\simeq 1.4$ and $\simeq 1.1$, respectively, comparable to the value inferred from our fit ($1.07^{+0.95}_{-0.47}$). Moreover, as mentioned in Section 3, the wavelength separation between Hγ and [O III] λ4363 is in principle resolvable at the PRISM spectral resolution in their observed wavelength range.

Nevertheless, given the limited S/N, we cannot completely exclude the possibility that imperfect deblending of Hγ and [O III] λ4363 substantially affects the inferred line fluxes. We therefore perform an additional test, assuming the Case B flux ratio between Hγ and Hδ. If part of the flux attributed to [O III] λ4363 in the fiducial fit is instead assigned to Hγ to satisfy Hγ/H$\delta = 1.8$, the inferred O3Hg ratio decreases to $-0.21^{+0.43}_{-0.53}$. This value could also be consistent with non-AGN ionization, depending on the O32 and Ne3O2 ratios, but is comparable to those observed in some LRDs and AGNs (B. E. Backhaus et al. 2025; G. C. Jones et al. 2026; M. Brazzini et al. 2026). Therefore, the limited wavelength coverage and depth of the available data prevent us from drawing a definitive conclusion about the nature of the ionizing source.

4.5. *Possible iron feature*

We find that there is also an emission-like feature at $\lambda_{\rm obs} \sim 2.7$ - $2.9\,\mu$m, corresponding to $\lambda_{\rm rest} \sim 0.24$ - $0.25\,\mu$m at $z = 10.36$. Fitting this feature with a single Gaussian (Section 3) gives $F_{\rm line} = 121.4^{+27.5}_{-27.2} \times 10^{-20}$ erg s^{-1} cm^{-2} (EW$_{\rm rest} = 79.2^{+18.8}_{-18.7}$ Å, $S/N = 4.4$) with a large FWHM of $1.22^{+0.58}_{-0.32} \times 10^4$ km s^{-1}. This feature may correspond to the Fe II UV bump or the Fe III UV47 multiplet, with no other prominent emission lines expected at this wavelength. Such iron emission lines are typically observed in quasars and are thought to originate from the broad-line region (BLR, e.g., B. J. Wills et al. 1980; M. Vestergaard & B. J. Wilkes 2001; T. A. A. Sigut et al. 2004). The large fitted FWHM is also consistent with an iron-line blend composed of multiple transitions.

Similar iron emission features have been reported in several LRDs (e.g., I. Labbe et al. 2024; X. Ji et al. 2026a; R. Tripodi et al. 2025), including detections from stacked spectra (e.g., P. G. Pérez-González et al. 2026; W. Q. Sun et al. 2026; M. Ando et al. 2026). In contrast, such features have not been commonly reported in normal star-forming galaxies at high redshift. If the observed feature is indeed due to iron emission, it would further support an AGN-powered LRD interpretation for CW-LRD-z10 and may suggest partial UV leakage from the central engine through a clumpy or porous envelope

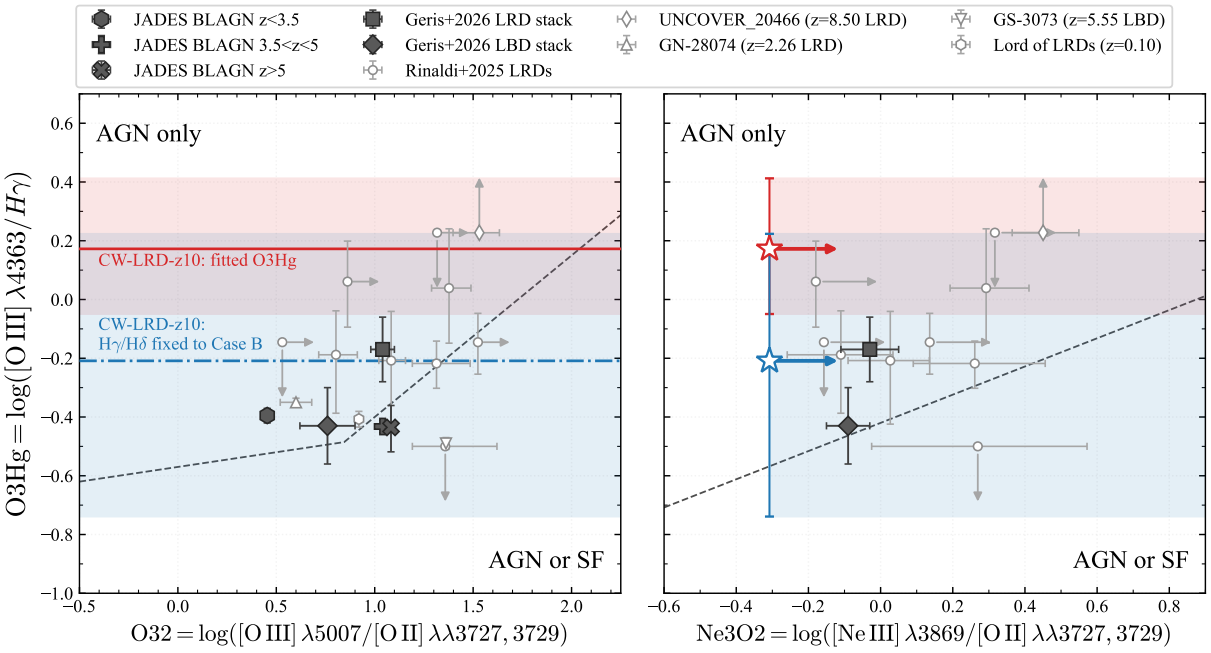


Figure 5. (left) O3Hg–O32 and (right) O3Hg–Ne3O2 line diagnostic diagrams. The black dashed line shows the empirical threshold proposed by G. Mazzolari et al. (2024), above which sources can be uniquely classified as AGNs ("AGN only"), while both AGNs and star-forming galaxies can occupy the region below ("AGN or SF"). In the left panel, the red solid and blue dot-dashed lines show the median O3Hg and the O3Hg after blending correction assuming the Case-B Balmer-line ratios between Hγ and Hδ. Note that no constraint on O32 is available because [O III] λ5007 falls outside the observed wavelength range. In the right panel, the stars and arrows indicate the conservative lower limit of Ne3O2, derived from the 3σ upper limit on the [O II] $\lambda\lambda$3727, 3729 flux and the 16th percentile of the [Ne III] λ3869 flux posterior. 1σ confidence levels are shown as the shaded regions. For comparison, we show the stacked spectra of JADES broad-line AGNs (I. Juodžbalis et al. 2025) and LRDs and LBDs (S. Geris et al. 2026) as gray filled markers, and individual sources from the literature as light-gray open markers: UNCOVER_20466 (G. C. Jones et al. 2026), GN-28074 and GS-3073 (M. Brazzini et al. 2026), the Lord of LRDs (X. Ji et al. 2026a), and the LRD sample from P. Rinaldi et al. (2024). Although the inferred line ratios are consistent with the AGN-only model and those observed in LRDs and AGNs, ionization by star formation cannot be ruled out given the uncertainties and possible line blending.

(M. Ando et al. 2026). Strong UV iron emission may also provide information on the physical conditions of the nuclear gas, since its strength depends sensitively on gas density, ionization parameter, column density, and radiative-transfer effects (e.g., R. Tripodi et al. 2025; A. Torralba et al. 2026; M. Ando et al. 2026). If confirmed as iron emission, this feature would suggest substantial chemical enrichment within the first $\sim$ 450 Myr of cosmic history. Both core-collapse supernovae and prompt Type Ia supernovae with short delay times of $\sim$ 30 - 100 Myr could have contributed to such early enrichment (e.g., F. Mannucci et al. 2006; D. Maoz et al. 2014; M. Nakane et al. 2024, 2025).

4.6. *Possible Lyα line*

As shown in Figure 2, the IGM+lines model overpredicts the continuum around $\lambda_{\rm obs}$ = 1.4 - 1.5 μm, and this remains the case even when fixing $x_{\rm HI}$ = 1.0, which maximizes the neutral IGM absorption. When using the IGM+lines model, Lyα emission is not detected (S/N = 0.5). In contrast, the IGM+CGM+lines model can reproduce the flux decrement using a strong Lyα damping-wing absorption with $\log\left(N_{\rm HI}/{\rm cm}^{-2}\right) = 22.81^{+0.20}_{-0.25}$ as seen in M. Ando et al. (2026). In this IGM+CGM+lines model, the excess flux around $\lambda_{\rm obs} \sim 1.4\,\mu$m can be explained by a Lyα emission line with S/N = 4.2. Lyα emission has also been reported in a number of LRDs in previous studies (e.g., Z. Ji et al. 2026; Y. Kageura et al. 2026; M. Ando et al. 2026).

A similar spectral feature of a Lyα line with a damping wing that cannot be explained by IGM-only models was reported even in a galaxy at z = 13.0 (J. Witstok et al. 2025). At such a high redshift, Lyα photons are expected to be strongly attenuated by the substantially neutral IGM; therefore, the detection of a Lyα line requires conditions that enhance Lyα transmission (e.g., M. Dijkstra 2014; M. Ouchi et al. 2020). One possibility is that the source resides in a large ionized bubble, within which Lyα photons can redshift away from resonance before encountering the neutral IGM (e.g., M. Tang et al. 2023; H. Umeda et al. 2024). Alternatively, radiative-transfer effects in the ISM and CGM, such as

resonant scattering and outflows, can shift Lyα photons redward of the systemic velocity and thereby enhance their transmission even through a smaller ionized region.

Thus, if the Lyα feature is real, it may indicate a locally ionized environment and/or favorable Lyα radiative-transfer conditions around CW-LRD-z10. However, the significance of the Lyα detection is model-dependent. Furthermore, the BIC improvement of the IGM+CGM+lines model relative to the IGM+lines model is only $\Delta\mathrm{BIC} = 2.6$, much less significant than the conventional $\Delta\mathrm{BIC} \gtrsim 10$ threshold for strong evidence. This indicates that the statistical preference for the CGM-included model is weak. We also note that the downturn around $\lambda_{\mathrm{obs}} \sim 1.4$ - $1.5\,\mu$m, reproduced by the IGM+CGM model in our fitting, may alternatively be consistent with nebular continuum emission (M. Ando et al. 2026). For these reasons, we do not conclude that the CGM-included model is preferred. Instead, we regard the Lyα detection as model-dependent and refrain from interpreting in detail the fitted parameters sensitive to the Lyα modeling, such as R_{b} and N_{HI}.

5. DISCUSSION: IS IT TRULY AN LRD?

In Section 4.1, we established that the source lies at $z = 10.36$ rather than being a low-redshift interloper. In this section, we discuss whether the observed SED at $z = 10.36$ necessarily requires an LRD interpretation, or whether it could instead arise from a non-LRD component.

There is currently no community-wide consensus on a definitive definition of LRDs. Nevertheless, three key characteristics are commonly used to identify them: a compact morphology, a V-shaped continuum with a minimum around or redward of the Balmer limit, and broad Balmer emission lines (e.g., R. E. Hviding et al. 2025; A. de Graaff et al. 2026). For CW-LRD-z10, T. S. Tanaka et al. (2025) confirmed its compact morphology, and, in this work, we spectroscopically confirm its redshift ($z_{\mathrm{spec}} = 10.36$, Section 4.1) and the presence of the characteristic V-shaped continuum, with its turnover at the Balmer limit (Section 4.2). However, broad Balmer lines have not yet been spectroscopically confirmed because Hβ and Hα fall outside the wavelength coverage of the current NIRSpec/PRISM spectrum (Figure 1). Although the possibly high [O III] λ4363/Hγ ratio (Section 4.4) and the possible iron emission (Section 4.5) support its LRD or AGN nature, an unambiguous spectroscopic confirmation has not yet been achieved.

We therefore consider whether the observed SED at $z = 10.36$ could instead be explained by a stellar-origin Balmer break. Such a model could in principle reproduce the turnover, and the iron complex and the high O3Hg ratio could arise from an AGN component. However, this alternative solution is strongly disfavored by the extremely red NIRCam-MIRI color of CW-LRD-z10, $m_{\mathrm{F444W}} - m_{\mathrm{F770W}} = 1.82$, based on its robust $S/N = 18$ detection in F770W (T. S. Tanaka et al. 2025). If the rest-frame optical continuum were approximately flat in f_ν from $\lambda_{\mathrm{rest}} \sim 0.4$ - $0.9\,\mu$m, as expected for a typical Balmer-break galaxy, reproducing the F770W flux would require an Hα rest-frame equivalent width (EW) of $\sim (6\pm1)\times10^3$ Å. Such an extreme EW is substantially larger than those expected theoretically ($\lesssim 4000$ Å; A. K. Inoue 2011) or typically observed in extreme emission line galaxies (~ 2000 Å; e.g., S. Withers et al. 2023). The F770W detection therefore provides important support for the LRD nature of CW-LRD-z10. We further confirm that CW-LRD-z10 is independently detected in each of the four individual COSMOS-Web F770W exposures prior to mosaicing, indicating that the F770W signal is unlikely to be caused by an imaging artifact.

Another possible explanation for the red rest-optical continuum is dust-reddened AGN emission (e.g., D. D. Kocevski et al. 2023; J. Matthee et al. 2024; J. E. Greene et al. 2024; P. Madau & R. Maiolino 2026; P. Madau et al. 2026). However, the observed turnover near the Balmer limit is characteristic of previously observed LRDs (D. J. Setton et al. 2025a; A. de Graaff et al. 2026), whereas such a coincidence is not necessarily expected from simple dust reddening. Furthermore, the tentative C IV and UV iron emission features, commonly associated with AGN activity, suggest that at least part of the nuclear UV emission is visible without severe obscuration. This may be in tension with a uniformly dust-obscured AGN, although more complex geometries involving partial covering or scattering, as well as non-standard dust attenuation curves (Z. Li et al. 2025), remain possible. Moreover, despite the ALMA non-detection (T. S. Tanaka et al. 2025), obscuration by dust hotter than that effectively probed by the available ALMA observations, or by a compact dust distribution with a small global covering factor, cannot be excluded (C. M. Casey et al. 2025; P. Madau & R. Maiolino 2026; I. Delvecchio et al. 2025). Similarly, the X-ray non-detection (T. S. Tanaka et al. 2025) does not rule out the possibility of a Compton-thick AGN. Therefore, while the observed properties are consistent with an LRD-like interpretation, we cannot rule out dust-obscured AGN scenarios with the current data. On the other hand, previous studies have not ruled out the possibility that dust attenuation also contributes to the red rest-optical continua of LRDs themselves (e.g., P. Madau & R. Maiolino 2026). Thus, dust-reddened AGN and other proposed LRD scenarios are not necessarily mutually exclusive, and it remains unclear whether they can

be observationally distinguished with the currently available data. Further observations at longer wavelengths are needed to distinguish between these scenarios and better constrain the physical origin of the red rest-optical continuum.

6. CONCLUSION

CW-LRD-z10 is a robust $z > 10$ LRD candidate with $z_{\rm phot} = 10.5^{+0.7}_{-0.6}$ selected from the COSMOS-Web dataset using a joint NIRCam-MIRI color selection (T. S. Tanaka et al. 2025). We present the NIRSpec/PRISM spectrum of CW-LRD-z10 (Figure 1) taken in the EMBER program. The key results are as follows:

- Based on the clearly detected Lyα break and emission lines with $S/N \sim 2$-4 (Figure 2), we spectroscopically measure the redshift as $z = 10.361^{+0.003}_{-0.002}$, consistent with the photometric redshift (Section 4.1). The corresponding UV absolute magnitude is $M_{\rm UV} = -20.16^{+0.07}_{-0.07}$, comparable to those of the most UV-luminous LRDs ever found (Figure 3). The $z_{\rm spec}$ confirmation removes the principal redshift uncertainty underlying the number density estimates in T. S. Tanaka et al. (2025).

- We spectroscopically confirm a V-shaped SED with UV and optical continuum slopes of $\beta_{\rm UV} = -2.26^{+0.11}_{-0.11}$ and $\beta_{\rm opt} = 1.17^{+0.74}_{-0.70}$, respectively (Section 4.2). The turnover wavelength, $\lambda_{\rm turn} = 0.356^{+0.010}_{-0.013}\,\mu$m, is consistent with the Balmer limit. Both of these findings satisfy key spectroscopic characteristics commonly associated with LRDs.

- Line detections are tentative with $S/N = 2$-4, and C IV $\lambda\lambda$1549, 1551 and [O III] λ4363 have the highest significances of $S/N = 3.9$ and 3.6, respectively. However, the stacking analysis provides additional support for the line interpretation (Figure 4, Section 4.3).

- The line fitting suggests a possibly high [O III] λ4363/Hγ flux ratio of O3Hg = log ([O III] λ4363/Hγ) $= 0.17^{+0.24}_{-0.22}$, or $-0.21^{+0.43}_{-0.53}$ after accounting for possible deblending between [O III] λ4363 and Hγ by imposing the Case B Balmer-line ratio between Hγ and Hδ (Figure 5, Section 4.4). These high line ratios are consistent with those previously observed in LRDs and AGNs, but do not rule out ionization by star formation.

- We detect a possible UV iron emission feature at $\lambda_{\rm rest} \sim 0.24$-$0.25\,\mu$m (Section 4.5). If confirmed as iron emission, this feature would be consistent with those observed in previously known AGNs and LRDs.

- We also find a possible, absorption-model-dependent detection of Lyα emission ($S/N = 4.2$ with the IGM+CGM model, Section 4.6) with a strong absorption feature that cannot be reproduced by IGM absorption alone. This may suggest enhanced Lyα transmission around CW-LRD-z10 even at $z_{\rm spec} = 10.36$.

- Due to the lack of spectroscopic confirmation of broad Balmer lines, the LRD nature of CW-LRD-z10 has not yet been established definitively. Nevertheless, when combined with the previously reported large $m_{\rm F444W} - m_{\rm F770W}$ color excess and the spectroscopic features presented here, the LRD interpretation provides the most plausible explanation for the observed properties of CW-LRD-z10 (Section 5). We therefore regard CW-LRD-z10 as the first $z > 10$ LRD candidate with a spectroscopically confirmed redshift.

The planned MIRI/LRS spectroscopy in Cycle 5 (GO#9483, PI T. S. Tanaka) will provide a deep mid-infrared spectrum covering Hα, Hβ, [O III] λ5007 and the rest-optical continuum, which will enable further tests and a more detailed characterization of its nature. Complementing the MIRI spectroscopy, deeper NIRSpec observations at higher spectral resolution will enable more detailed spectroscopic characterization through more robust line detections, improved Lyα and IGM+CGM modeling, and more reliable photoionization modeling.

To constrain the evolution of the LRD population, we need a larger $z > 10$ LRD sample, which requires more extensive MIRI observations. Beyond *JWST*-only searches, future MIRI follow-up of bright $z > 10$ candidates identified by the recently launched *Roman* Space Telescope will be effective for searching for more luminous $z > 10$ LRDs over much wider areas. On a longer timescale, the proposed *GREX-PLUS* mission will further extend such searches through its wide-field near- to mid-infrared imaging capabilities (GREX-PLUS Science Team et al. 2023; A. K. Inoue et al. 2024; GREX-PLUS Science Team et al. 2026).

ACKNOWLEDGEMENTS

This work is based on observations made with the NASA/ESA/CSA *James Webb Space Telescope*. The data were obtained from the Mikulski Archive for Space Telescopes at the Space Telescope Science Institute, which is operated by the Association of Universities

for Research in Astronomy, Inc., under NASA contract NAS5-03127 for JWST. These observations are associated with program GO-7076. Support for US investigators in program GO-7076 was provided by NASA through a grant from the Space Telescope Science Institute, which is operated by the Association of Universities for Research in Astronomy, Inc., under NASA contract NAS5-03127. The observation can be accessed via doi: 10.17909/7mg3-kh29. Numerical computations were in part carried out on the iDark cluster, Kavli IPMU. This work was made possible by utilizing the CANDIDE cluster at the Institut d'Astrophysique de Paris. The CANDIDE cluster was funded through grants from the PNCG, CNES, DIM-ACAV, the Euclid Consortium, and the Danish National Research Foundation Cosmic Dawn Center (DNRF140) and is maintained by Stephane Rouberol. The COSMOS team is partly supported by the Centre National d'Etudes Spatiales (CNES). Kavli IPMU is supported by World Premier International Research Center Initiative (WPI), MEXT, Japan. The Cosmic Dawn Center is funded by the Danish National Research Foundation (DNRF140). We thank Yoshihisa Asada, Ignas Juodžbalis, and Lucy R. Ivey for fruitful discussion. We thank the anonymous referee for helpful feedback. T. S. Tanaka is supported by Japan Society for the Promotion of Science (JSPS) KAKENHI Grant Number JP25KJ0750 and the Forefront Physics and Mathematics Program to Drive Transformation (FoPM), a World-leading Innovative Graduate Study (WINGS) Program at the University of Tokyo. T. S. Tanaka gratefully acknowledges UNISON SQUARE GARDEN, whose full-color music motivated him throughout this research and inspired him to keep surprising the world. M. Aravena is supported by FONDECYT grant number 1252054, and gratefully acknowledges support from ANID Basal Project FB210003, ANID MILENIO NCN2024_112 and ANID + Vinculación Internacional + FOVI250261. B. Trakhtenbrot acknowledges support from the European Research Council (ERC) under the European Union's Horizon 2020 research and innovation program (grant agreement No. 950533). K. Inayoshi acknowledges support from the National Natural Science Foundation of China (12573015, W2532003), the Beijing Natural Science Foundation (IS25003), and the China Manned Space Program (CMS-CSST-2025-A09). J.-T. Schindler acknowledges funding by the Deutsche Forschungsgemeinschaft (DFG, German Research Foundation) - Project number 518006966 - and support by the DFG under Germany's Excellence Strategy – EXC 2121 „Quantum Universe" – 390833306. A. K. Inoue is supported by Japan Society for the Promotion of Science (JSPS) KAKENHI Grant Number JP26H02069. O. Ilbert acknowledges the funding of the French Agence Nationale de la Recherche for the project iMAGE (grant ANR-22-CE31-0007). D. B. Sanders gratefully acknowledges support from NSF Grant 2407752. E. Treister acknowledges support from the ANID CATA-BASAL program FB210003, and FONDECYT Regular 1241005 and 1250821. OpenAI ChatGPT was used under author supervision to assist with language editing and refinement of the manuscript text. All scientific content, interpretations, references, and final wording were reviewed and approved by the authors, who take full responsibility for the content of the manuscript.

REFERENCES

Planck Collaboration, Aghanim, N., Akrami, Y., et al. 2020, A&A, 641, A6, doi: 10.1051/0004-6361/201833910

Akins, H. B., Casey, C. M., Lambrides, E., et al. 2025, ApJ, 991, 37, doi: 10.3847/1538-4357/ade984

Ananna, T. T., Bogdán, Á., Kovács, O. E., Natarajan, P., & Hickox, R. C. 2024, ApJL, 969, L18, doi: 10.3847/2041-8213/ad5669

Ando, M., Harikane, Y., Katz, H., Inayoshi, K., & Tanaka, T. S. 2026, arXiv e-prints, arXiv:2606.03522, doi: 10.48550/arXiv.2606.03522

Backhaus, B. E., Cleri, N. J., Trump, J. R., et al. 2025, ApJ, 994, 125, doi: 10.3847/1538-4357/ae1136

Barro, G., Pérez-González, P. G., Kocevski, D. D., et al. 2024, ApJ, 963, 128, doi: 10.3847/1538-4357/ad167e

Barro, G., Pérez-González, P. G., Kocevski, D., et al. 2026, ApJ, 1003, 96, doi: 10.3847/1538-4357/ae5d2c

Brazzini, M., D'Eugenio, F., Maiolino, R., et al. 2026, arXiv e-prints, arXiv:2601.22214, doi: 10.48550/arXiv.2601.22214

Brooks, M., Davis, K., Trump, J. R., et al. 2026, arXiv e-prints, arXiv:2608.12487, doi: 10.48550/arXiv.2608.12487

Bushouse, H., Eisenhamer, J., Dencheva, N., et al. 2023, Zenodo, doi: 10.5281/zenodo.8380331

Cai, X., Inoue, A. K., Onoue, M., et al. 2026, arXiv e-prints, arXiv:2610.28735, doi: 10.48550/arXiv.2610.28735

Casey, C. M., Kartaltepe, J. S., Drakos, N. E., et al. 2023, ApJ, 954, 31, doi: 10.3847/1538-4357/acc2bc

Casey, C. M., Akins, H. B., Finkelstein, S. L., et al. 2025, arXiv e-prints, arXiv:2505.18873, doi: 10.48550/arXiv.2505.18873

Chang, S.-J., Gronke, M., Matthee, J., & Mason, C. 2026, MNRAS, 545, staf2131, doi: 10.1093/mnras/staf2131

Chen, C.-H., Shangguan, J., Ho, L. C., et al. 2026, arXiv e-prints, arXiv:2606.04711, doi: 10.48550/arXiv.2606.04711

de Graaff, A., Rix, H.-W., Carniani, S., et al. 2024, A&A, 684, A87, doi: 10.1051/0004-6361/202347755

de Graaff, A., Rix, H.-W., Naidu, R. P., et al. 2025a, A&A, 701, A168, doi: 10.1051/0004-6361/202554681

de Graaff, A., Brammer, G., Weibel, A., et al. 2025b, A&A, 697, A189, doi: 10.1051/0004-6361/202452186

de Graaff, A., Hviding, R. E., Naidu, R. P., et al. 2026, MNRAS, doi: 10.1093/mnras/stag1567

Delvecchio, I., Daddi, E., Magnelli, B., et al. 2025, A&A, 704, A313, doi: 10.1051/0004-6361/202557164

Dijkstra, M. 2014, PASA, 31, e040, doi: 10.1017/pasa.2014.33

Feltre, A., Charlot, S., & Gutkin, J. 2016, MNRAS, 456, 3354, doi: 10.1093/mnras/stv2794

Foreman-Mackey, D., Hogg, D. W., Lang, D., & Goodman, J. 2013, PASP, 125, 306, doi: 10.1086/670067

Fu, S., Zhang, Z., Jiang, D., et al. 2026, Nature Astronomy, 10, 1372, doi: 10.1038/s41550-026-02885-8

Furtak, L. J., Labbé, I., Zitrin, A., et al. 2024, Nature, 628, 57, doi: 10.1038/s41586-024-07184-8

Furtak, L. J., Secunda, A. R., Greene, J. E., et al. 2025, A&A, 698, A227, doi: 10.1051/0004-6361/202554110

Geris, S., Maiolino, R., Ji, X., et al. 2026, arXiv e-prints, arXiv:2606.21614, doi: 10.48550/arXiv.2606.21614

Gloudemans, A. J., Duncan, K. J., Eilers, A.-C., et al. 2025, ApJ, 986, 130, doi: 10.3847/1538-4357/adddb9

Greene, J. E., Labbe, I., Goulding, A. D., et al. 2024, ApJ, 964, 39, doi: 10.3847/1538-4357/ad1e5f

GREX-PLUS Science Team, Inoue, A. K., Harikane, Y., et al. 2023, arXiv e-prints, arXiv:2304.08104, doi: 10.48550/arXiv.2304.08104

GREX-PLUS Science Team, Baba, S., Belli, S., et al. 2026, arXiv e-prints, arXiv:2606.05237, doi: 10.48550/arXiv.2606.05237

Gutkin, J., Charlot, S., & Bruzual, G. 2016, MNRAS, 462, 1757, doi: 10.1093/mnras/stw1716

Hainline, K. N., Maiolino, R., Juodžbalis, I., et al. 2025, ApJ, 979, 138, doi: 10.3847/1538-4357/ad9920

Harikane, Y., Zhang, Y., Nakajima, K., et al. 2023, ApJ, 959, 39, doi: 10.3847/1538-4357/ad029e

Horne, K. 1986, Publications of the Astronomical Society of the Pacific, 98, 609, doi: 10.1086/131801

Hviding, R. E. 2026, unite: Unified liNe Integration Turbo Engine, v3.5.0 Zenodo, doi: 10.5281/zenodo.23366301

Hviding, R. E., de Graaff, A., Miller, T. B., et al. 2025, A&A, 702, A57, doi: 10.1051/0004-6361/202555816

Hviding, R. E., de Graaff, A., Liu, H., et al. 2026, ApJL, 1000, L18, doi: 10.3847/2041-8213/ae4c88

Inayoshi, K. 2025, ApJL, 988, L22, doi: 10.3847/2041-8213/adea66

Inayoshi, K., & Ho, L. C. 2025, arXiv e-prints, arXiv:2512.03130, doi: 10.48550/arXiv.2512.03130

Inayoshi, K., & Maiolino, R. 2025, ApJL, 980, L27, doi: 10.3847/2041-8213/adaebd

Inayoshi, K., Murase, K., & Kashiyama, K. 2026, ApJ, 1000, 90, doi: 10.3847/1538-4357/ae42ce

Inayoshi, K., Visbal, E., & Haiman, Z. 2020, Annual Review of Astronomy and Astrophysics, 58, 27, doi: 10.1146/annurev-astro-120419-014455

Inoue, A. K. 2011, MNRAS, 415, 2920, doi: 10.1111/j.1365-2966.2011.18906.x

Inoue, A. K., Yamamura, I., Suzuki, T., et al. 2024, in Society of Photo-Optical Instrumentation Engineers (SPIE) Conference Series, Vol. 13092, Space Telescopes and Instrumentation 2024: Optical, Infrared, and Millimeter Wave, ed. L. E. Coyle, S. Matsuura, & M. D. Perrin, 130920Y, doi: 10.1117/12.3017780

Ji, X., Maiolino, R., Übler, H., et al. 2025, MNRAS, 544, 3900, doi: 10.1093/mnras/staf1867

Ji, X., D'Eugenio, F., Juodžbalis, I., et al. 2026a, MNRAS, 545, staf2235, doi: 10.1093/mnras/staf2235

Ji, X., Pezzulli, G., D'Eugenio, F., et al. 2026b, arXiv e-prints, arXiv:2604.03370, doi: 10.48550/arXiv.2604.03370

Ji, Z., Sun, Y., Giavalisco, M., et al. 2026, arXiv e-prints, arXiv:2606.09970, doi: 10.48550/arXiv.2606.09970

Johnson, B. D., Leja, J., Conroy, C., & Speagle, J. S. 2021, ApJS, 254, 22, doi: 10.3847/1538-4365/abef67

Jones, G. C., Übler, H., Maiolino, R., et al. 2026, MNRAS, 546, stag115, doi: 10.1093/mnras/stag115

Juodžbalis, I., Maiolino, R., Baker, W. M., et al. 2025, arXiv e-prints, arXiv:2504.03551, doi: 10.48550/arXiv.2504.03551

Kageura, Y., Ouchi, M., Yanagisawa, H., et al. 2026, arXiv e-prints, arXiv:2608.14534, doi: 10.48550/arXiv.2608.14534

Kido, D., Ioka, K., Hotokezaka, K., Inayoshi, K., & Irwin, C. M. 2025, MNRAS, 544, 3407, doi: 10.1093/mnras/staf1898

Kocevski, D. D., Onoue, M., Inayoshi, K., et al. 2023, ApJL, 954, L4, doi: 10.3847/2041-8213/ace5a0

Kocevski, D. D., Finkelstein, S. L., Barro, G., et al. 2025, ApJ, 986, 126, doi: 10.3847/1538-4357/adbc7d

Kocevski, D. D., Taylor, A. J., Onoue, M., et al. 2026, arXiv e-prints, arXiv:2609.00112. https://arxiv.org/abs/2609.00112

Kokorev, V., Chisholm, J., Endsley, R., et al. 2024, ApJ, 975, 178, doi: 10.3847/1538-4357/ad7d03

Kokubo, M., & Harikane, Y. 2025, ApJ, 995, 24, doi: 10.3847/1538-4357/ae119e

Kormendy, J., & Ho, L. C. 2013, ARA&A, 51, 511, doi: 10.1146/annurev-astro-082708-101811

Labbé, I., van Dokkum, P., Nelson, E., et al. 2023, Nature, 616, 266, doi: 10.1038/s41586-023-05786-2

Labbe, I., Greene, J. E., Matthee, J., et al. 2024, arXiv e-prints, arXiv:2412.04557, doi: 10.48550/arXiv.2412.04557

Labbe, I., Greene, J. E., Bezanson, R., et al. 2025, ApJ, 978, 92, doi: 10.3847/1538-4357/ad3551

Lambrides, E., Hutchison, T. A., Larson, R. L., et al. 2026, arXiv e-prints, arXiv:2604.25991, doi: 10.48550/arXiv.2604.25991

Li, Z., Inayoshi, K., Chen, K., Ichikawa, K., & Ho, L. C. 2025, ApJ, 980, 36, doi: 10.3847/1538-4357/ada5fb

Lin, R., Zheng, Z.-Y., Wang, J., et al. 2026, ApJ, 1005, 150, doi: 10.3847/1538-4357/ae74c6

Lin, X., Fan, X., Cai, Z., et al. 2026a, ApJ, 997, 364, doi: 10.3847/1538-4357/ae2bdf

Lin, X., Fan, X., Wang, F., et al. 2026b, ApJ, 996, 93, doi: 10.3847/1538-4357/ae1b9b

Liu, Z., Naidu, R. P., Secunda, A., et al. 2026, arXiv e-prints, arXiv:2604.13000, doi: 10.48550/arXiv.2604.13000

Madau, P., & Maiolino, R. 2026, arXiv e-prints, arXiv:2602.22386, doi: 10.48550/arXiv.2602.22386

Madau, P., Maiolino, R., & D'Eugenio, F. 2026, arXiv e-prints, arXiv:2609.06239, doi: 10.48550/arXiv.2609.06239

Maiolino, R., Risaliti, G., Signorini, M., et al. 2025, MNRAS, 538, 1921, doi: 10.1093/mnras/staf359

Mannucci, F., Della Valle, M., & Panagia, N. 2006, MNRAS, 370, 773, doi: 10.1111/j.1365-2966.2006.10501.x

Maoz, D., Mannucci, F., & Nelemans, G. 2014, ARA&A, 52, 107, doi: 10.1146/annurev-astro-082812-141031

Martin, C. L., Hu, W., Wold, I. G. B., et al. 2026, ApJ, 997, 102, doi: 10.3847/1538-4357/ae1d6b

Matthee, J., Naidu, R. P., Brammer, G., et al. 2024, ApJ, 963, 129, doi: 10.3847/1538-4357/ad2345

Mazzolari, G., Übler, H., Maiolino, R., et al. 2024, A&A, 691, A345, doi: 10.1051/0004-6361/202450407

Mazzolari, G., Gilli, R., Maiolino, R., et al. 2026, A&A, 706, A372, doi: 10.1051/0004-6361/202453317

Miralda-Escudé, J. 1998, ApJ, 501, 15, doi: 10.1086/305799

Naidu, R. P., Matthee, J., Katz, H., et al. 2026, Nature, 656, 329, doi: 10.1038/s41586-026-10846-4

Nakane, M., Ouchi, M., Nakajima, K., et al. 2024, ApJ, 976, 122, doi: 10.3847/1538-4357/ad84e8

Nakane, M., Ouchi, M., Nakajima, K., et al. 2025, ApJ, 994, 65, doi: 10.3847/1538-4357/ae04e6

Nikopoulos, G. P., Watson, D., Sneppen, A., et al. 2026, A&A, 710, A136, doi: 10.1051/0004-6361/202557604

Ouchi, M., Ono, Y., & Shibuya, T. 2020, ARA&A, 58, 617, doi: 10.1146/annurev-astro-032620-021859

Pacucci, F., Ferrara, A., & Kocevski, D. D. 2026, arXiv e-prints, arXiv:2601.14368, doi: 10.48550/arXiv.2601.14368

Pang, Y., Wang, X., Cheng, C., et al. 2026, ApJ, 1004, 185, doi: 10.3847/1538-4357/ae6e3f

Pérez-González, P. G., Barro, G., Carniani, S., et al. 2026, arXiv e-prints, arXiv:2602.20247, doi: 10.48550/arXiv.2602.20247

Perger, K., Fogasy, J., Frey, S., & Gabányi, K. É. 2025, A&A, 693, L2, doi: 10.1051/0004-6361/202452422

Regan, J., & Volonteri, M. 2024, The Open Journal of Astrophysics, 7, 72, doi: 10.33232/001c.123239

Rigby, J., Perrin, M., McElwain, M., et al. 2023, PASP, 135, 048001, doi: 10.1088/1538-3873/acb293

Rinaldi, P., Bonaventura, N., Rieke, G. H., et al. 2024, arXiv e-prints, arXiv:2411.14383, doi: 10.48550/arXiv.2411.14383

Rodriguez, L. F., & Mirabel, I. F. 2026, A&A, 707, L17, doi: 10.1051/0004-6361/202558326

Rodríguez, L. F., Mirabel, I. F., González-Lópezlira, R. A., & Loinard, L. 2026, ApJ, 1009, 217, doi: 10.3847/1538-4357/ae9b01

Rusakov, V., Watson, D., Nikopoulos, G. P., et al. 2025, arXiv e-prints, arXiv:2503.16595, doi: 10.48550/arXiv.2503.16595

Setton, D. J., Greene, J. E., de Graaff, A., et al. 2025a, ApJ, 995, 118, doi: 10.3847/1538-4357/ae1500

Setton, D. J., Greene, J. E., Spilker, J. S., et al. 2025b, ApJL, 991, L10, doi: 10.3847/2041-8213/ade78b

Sigut, T. A. A., Pradhan, A. K., & Nahar, S. N. 2004, ApJ, 611, 81, doi: 10.1086/422027

Sneppen, A., Watson, D., Matthews, J. H., et al. 2026a, arXiv e-prints, arXiv:2601.18864, doi: 10.48550/arXiv.2601.18864

Sneppen, A., Matthews, J. H., Watson, D., et al. 2026b, arXiv e-prints, arXiv:2604.09399, doi: 10.48550/arXiv.2604.09399

Stone, Z., Shen, Y., Zhuang, M.-Y., et al. 2026, arXiv e-prints, arXiv:2608.01647, doi: 10.48550/arXiv.2608.01647

Sun, W. Q., Naidu, R. P., Matthee, J., et al. 2026, The Open Journal of Astrophysics, 9, 62505, doi: 10.33232/001c.162505

Tanaka, T. S., Akins, H. B., Harikane, Y., et al. 2025, ApJ, 995, 21, doi: 10.3847/1538-4357/ae145f

Tang, M., Stark, D. P., Chen, Z., et al. 2023, MNRAS, 526, 1657, doi: 10.1093/mnras/stad2763

Tang, M., Stark, D. P., Mason, C. A., et al. 2026, arXiv e-prints, arXiv:2604.03563, doi: 10.48550/arXiv.2604.03563

Taylor, A. J., Kokorev, V., Kocevski, D. D., et al. 2025, arXiv e-prints, arXiv:2505.04609, doi: 10.48550/arXiv.2505.04609

Tee, W. L., Fan, X., Wang, F., & Yang, J. 2025, ApJL, 983, L26, doi: 10.3847/2041-8213/adc5e3

Torralba, A., Matthee, J., Pezzulli, G., et al. 2026, A&A, 707, A75, doi: 10.1051/0004-6361/202557537

Totani, T., Kawai, N., Kosugi, G., et al. 2006, PASJ, 58, 485, doi: 10.1093/pasj/58.3.485

Tripodi, R., Bradač, M., D'Eugenio, F., et al. 2025, ApJL, 994, L6, doi: 10.3847/2041-8213/ae13a9

Umeda, H., Inayoshi, K., Harikane, Y., & Murase, K. 2026, ApJ, 999, 183, doi: 10.3847/1538-4357/ae4101

Umeda, H., Ouchi, M., Nakajima, K., et al. 2024, ApJ, 971, 124, doi: 10.3847/1538-4357/ad554e

Vestergaard, M., & Wilkes, B. J. 2001, ApJS, 134, 1, doi: 10.1086/320357

Volonteri, M. 2010, A&A Rv, 18, 279, doi: 10.1007/s00159-010-0029-x

Wang, B., de Graaff, A., Davies, R. L., et al. 2025, ApJ, 984, 121, doi: 10.3847/1538-4357/adc1ca

Wills, B. J., Netzer, H., & Wills, D. 1980, ApJL, 242, L1, doi: 10.1086/183388

Withers, S., Muzzin, A., Ravindranath, S., et al. 2023, ApJL, 958, L14, doi: 10.3847/2041-8213/ad01c0

Witstok, J., Jakobsen, P., Maiolino, R., et al. 2025, Nature, 639, 897, doi: 10.1038/s41586-025-08779-5

Yan, Z., Inayoshi, K., Chen, K., & Guo, J. 2026, ApJ, 1002, 159, doi: 10.3847/1538-4357/ae5dbd

Yanagisawa, H., Ouchi, M., Kiyota, T., et al. 2026, arXiv e-prints, arXiv:2606.09726, doi: 10.48550/arXiv.2606.09726

Yue, M., Eilers, A.-C., Ananna, T. T., et al. 2024, ApJL, 974, L26, doi: 10.3847/2041-8213/ad7eba

Zhang, Z., Jiang, L., Liu, W., & Ho, L. C. 2025a, ApJ, 985, 119, doi: 10.3847/1538-4357/adcb3e

Zhang, Z., Li, M., Oguri, M., et al. 2025b, arXiv e-prints, arXiv:2512.05180, doi: 10.48550/arXiv.2512.05180

Zhou, S., Sun, M., Zhang, Z., Chen, J., & Ho, L. C. 2025, ApJ, 991, 137, doi: 10.3847/1538-4357/adfd5f

Zhou, S., Sun, M., Ji, X., et al. 2026, arXiv e-prints, arXiv:2606.21105, doi: 10.48550/arXiv.2606.21105

All Authors and Affiliations

Takumi S. Tanaka,[1,2,3] Hollis B. Akins,[4,*] John D. Silverman,[1,2,3,5] Caitlin M. Casey,[6,7] Ezequiel Treister,[8] Manuel Aravena,[9,10] Yuichi Harikane,[11] Benny Trakhtenbrot,[12] Kohei Inayoshi,[13] Kazuhiro Shimasaku,[2,14] Maximilien Franco,[15] Seiji Fujimoto,[16,17] Mingyu Li,[18,19,20] Hiroya Umeda,[21] Jan-Torge Schindler,[22] Akio K. Inoue,[23,24] Jean-Baptiste Billand,[15] Darshan Kakkad,[25] Xuheng Ding,[26] Steven L. Finkelstein,[27,28] Michaela Hirschmann,[29,30] Z. Ghaffari,[31,32] Andrew J. Battisti,[33,34] Lauro Moscardini,[35,36,37] Nicole E. Drakos,[38] Rasha M. Samir,[39] Jeyhan S. Kartaltepe,[40] Qinyue Fei,[16] Ming-Yang Zhuang,[41] Olivier Ilbert,[42] Wuji Wang,[43] Rafael C. Arango-Toro,[44] Hiddo S. B. Algera,[45] Greta Toni,[35,36,46] Junya Arita,[2] Kei Ito,[7,47] Ghassem Gozaliasl,[48,49] Dale D. Kocevski,[50] Yunjing Wu,[1,3] Masafusa Onoue,[51,1] Marc Huertas-Company,[52,53,54,55] Yiyang Zhang,[26] Jason Rhodes,[56] Andreas L. Faisst,[43] Zihao Li,[7,57] Crystal L. Martin,[6] Makoto Ando,[11] Vasily Kokorev,[58] Sophie L. Newman,[59] Can Xu,[60,61] Suin Matsui,[2] Jialai Wang,[62,63,1,3] Carter Flayhart,[40] Hossein Hatamnia,[64,65] Ali Ahmad Khostovan,[66,40] Ronaldo Laishram,[67] Felix Martinez III,[40] David B. Sanders,[68] Sune Toft,[7,57] Francesco Valentino[7,47] And Jorge Zavala[69]

(Affiliations can be found after the references)

[1]*Kavli Institute for the Physics and Mathematics of the Universe (WPI), The University of Tokyo Institutes for Advanced Study, The University of Tokyo, Kashiwa, Chiba 277-8583, Japan*

[2]*Department of Astronomy, Graduate School of Science, The University of Tokyo, 7-3-1 Hongo, Bunkyo-ku, Tokyo 113-0033, Japan*

[3]*Center for Data-Driven Discovery, Kavli IPMU (WPI), UTIAS, The University of Tokyo, Kashiwa, Chiba 277-8583, Japan*

[4]*Department of Astrophysical Sciences, Princeton University, 4 Ivy Lane, Princeton, NJ 08544, USA*

[5]*Center for Astrophysical Sciences, Department of Physics & Astronomy, Johns Hopkins University, Baltimore, MD 21218, USA*

[6]*Department of Physics, University of California, Santa Barbara, CA 93106, USA*

[7]*Cosmic Dawn Center (DAWN), Denmark*

[8]*Instituto de Alta Investigación, Universidad de Tarapacá, Casilla 7D, Arica, Chile*

[9]*Instituto de Estudios Astrofícos, Facultad de Ingeniería y Ciencias, Universidad Diego Portales, Av. Ejército 441, Santiago, Chile*

[10]*Millenium Nucleus for Galaxies (MINGAL)*

[11]*Institute for Cosmic Ray Research, The University of Tokyo, 5-1-5 Kashiwanoha, Kashiwa, Chiba 277-8582, Japan*

[12]*School of Physics and Astronomy, Tel Aviv University, Tel Aviv 69978, Israel*

[13]*Kavli Institute for Astronomy and Astrophysics, Peking University, Beijing 100871, China*

[14]*Research Center for the Early Universe, Graduate School of Science, The University of Tokyo, 7-3-1 Hongo, Bunkyo-ku, Tokyo 113-0033, Japan*

[15]*Université Paris-Saclay, Université Paris Cité, CEA, CNRS, AIM, 91191, Gif-sur-Yvette, France*

[16]*David A. Dunlap Department of Astronomy and Astrophysics, University of Toronto, 50 St. George Street, Toronto, Ontario, M5S 3H4, Canada*

[17]*Dunlap Institute for Astronomy and Astrophysics, 50 St. George Street, Toronto, Ontario, M5S 3H4, Canada*

[18]*Department of Astronomy, Tsinghua University, Beijing 100084, China*

[19]*Kavli Institute for Cosmology, University of Cambridge, Madingley Road, Cambridge CB3 0HA, UK*

[20]*Cavendish Laboratory, University of Cambridge, 19 JJ Thomson Avenue, Cambridge CB3 0HE, UK*

[21]*Center for Computational Sciences, University of Tsukuba, Ten-nodai, 1-1-1 Tsukuba, Ibaraki 305-8577, Japan*

[22]*Hamburger Sternwarte, University of Hamburg, Gojenbergsweg 112, D-21029 Hamburg, Germany*

[23]*Department of Pure and Applied Physics, Graduate School of Advanced Science and Engineering, Faculty of Science and Engineering, Waseda University, 3-4-1 Okubo, Shinjuku, Tokyo 169-8555, Japan*

[24]*Waseda Research Institute for Science and Engineering, Faculty of Science and Engineering, Waseda University, 3-4-1 Okubo, Shinjuku, Tokyo 169-8555, Japan*

[25]*Centre for Astrophysics Research, University of Hertfordshire, Hatfield, AL10 9AB, UK*

[26]*School of Physics and Technology, Wuhan University, Wuhan 430072, China*

[27]*Department of Astronomy, The University of Texas at Austin, Austin, TX, USA*

[28]*Cosmic Frontier Center, The University of Texas at Austin, Austin, TX, USA*

[29]*Institute of Physics, GalSpec, Ecole Polytechnique Federale de Lausanne, Observatoire de Sauverny, Chemin Pegasi 51, 1290 Versoix, Switzerland*

[30]*INAF, Astronomical Observatory of Trieste, Via Tiepolo 11, 34131 Trieste, Italy*

[31]*INAF Osservatorio Astronomico di Trieste, Via G.B. Tiepolo 11 e via Bazzoni 2. 34100, Trieste, Italy*

[32]*IFPU: Institute for Fundamental Physics of the Universe, Via Beirut, 2, 34151, Trieste, Italy*

[33]*International Centre for Radio Astronomy Research, University of Western Australia, 7 Fairway, Crawley, WA 6009, Australia*

[34]*Research School of Astronomy and Astrophysics, Australian National University, Cotter Road, Weston Creek, ACT 2611, Australia*

[35]*University of Bologna - Department of Physics and Astronomy "Augusto Righi" (DIFA), Via Gobetti 93/2, I-40129 Bologna, Italy*

[36]*INAF- Osservatorio di Astrofisica e Scienza dello Spazio, Via Gobetti 93/3, I-40129, Bologna, Italy*

[37]*INFN- Sezione di Bologna, Viale Berti Pichat 6/2, I-40127 Bologna, Italy*

[38]*Department of Physics and Astronomy, University of Hawaii, Hilo, 200 W Kawili St, Hilo, HI 96720, USA*
[39]*Department of Astronomy, National Research Institute of Astronomy and Geophysics (NRIAG), Cairo, 11421, Egypt*
[40]*Laboratory for Multiwavelength Astrophysics, School of Physics and Astronomy, Rochester Institute of Technology, 84 Lomb Memorial Drive, Rochester, NY 14623, USA*
[41]*Department of Astronomy, University of Illinois Urbana-Champaign, Urbana, IL 61801, USA*
[42]*Aix Marseille Univ, CNRS, CNES, LAM, Marseille, France*
[43]*IPAC, California Institute of Technology, 1200 E. California Blvd. Pasadena, CA 91125, USA*
[44]*Institut d'Astrophysique de Paris, UMR 7095, CNRS, and Sorbonne Université, 98bis boulevard Arago, 75014 Paris, France*
[45]*Institute of Astronomy and Astrophysics, Academia Sinica, 11F of Astronomy-Mathematics Building, No.1, Section 4, Roosevelt Rd, Taipei 106319, Taiwan, R.O.C*
[46]*Zentrum für Astronomie, Universität Heidelberg, Philosophenweg 12, D-69120, Heidelberg, Germany*
[47]*DTU Space, Technical University of Denmark, Elektrovej 327 DK2800 Kgs. Lyngby, Denmark*
[48]*Department of Computer Science, Aalto University, P.O. Box 15400, FI-00076 Espoo, Finland*
[49]*Department of Physics, University of Helsinki, P.O. Box 64, FI-00014 Helsinki, Finland*
[50]*Department of Physics and Astronomy, Colby College, Waterville, ME 04901, USA*
[51]*Waseda Institute for Advanced Study (WIAS), Waseda University, 1-21-1, Nishi-Waseda, Shinjuku, Tokyo 169-0051, Japan*
[52]*Instituto de Astrofísica de Canarias (IAC), La Laguna, E-38205, Spain*
[53]*Universidad de La Laguna. Avda. Astrofísico Fco. Sanchez, La Laguna, Tenerife, Spain*
[54]*Observatoire de Paris, LUX, PSL University, 61 avenue de l'Observatoire, F-75014 Paris, France*
[55]*Université de Paris, 5 Rue Thomas Mann, 75014 Paris, France*
[56]*Jet Propulsion Laboratory, California Institute of Technology, 4800 Oak Grove Drive, Pasadena, CA 91001, USA*
[57]*Niels Bohr Institute, University of Copenhagen, Jagtvej 128, DK2200 Copenhagen N, Denmark*
[58]*Kapteyn Astronomical Institute, University of Groningen, PO Box 800, 9700 AV Groningen, The Netherlands*
[59]*Institute of Cosmology and Gravitation, University of Portsmouth, Dennis Sciama Building, Burnaby Road, Portsmouth, PO1 3FX, UK*
[60]*School of Astronomy and Space Science, Nanjing University, Nanjing, Jiangsu 210093, China*
[61]*Key Laboratory of Modern Astronomy and Astrophysics, Nanjing University, Ministry of Education, Nanjing 210093, China*
[62]*Department of Astronomy, University of Science and Technology of China, Hefei 230026, China*
[63]*School of Astronomy and Space Science, University of Science and Technology of China, Hefei 230026, China*
[64]*Department of Physics and Astronomy, University of California, Riverside, 900 University Avenue, Riverside, CA 92521, USA*
[65]*Observatories of the Carnegie Institution for Science, 813 Santa Barbara St., Pasadena, CA 91101, USA*
[66]*Department of Physics and Astronomy, University of Kentucky, 505 Rose Street, Lexington, KY 40506, USA*
[67]*National Astronomical Observatory of Japan, 2-21-1 Osawa, Mitaka, Tokyo 181-8588, Japan*
[68]*Institute for Astronomy, University of Hawaii, 2680 Woodlawn Drive, Honolulu, HI 96822, USA*
[69]*Department of Astronomy, University of Massachusetts Amherst, 710 N Pleasant Street, Amherst, MA 01003, USA*